H^∞ Repetitive Control of DC-AC Converters in Microgrids

George Weiss, Qing-Chang Zhong, Tim C. Green, *Senior Member, IEEE*, and Jun Liang, *Member, IEEE*

***Abstract*—This paper proposes a voltage controller design method for dc–ac converters supplying power to a microgrid, which is also connected to the power grid. This converter is meant to operate in conjunction with a small power generating unit. The design of the output voltage controller is based on H^∞ and repetitive control techniques. This leads to a very low harmonic distortion of the output voltage, even in the presence of nonlinear loads and/or grid distortions. The output voltage controller contains an infinite-dimensional internal model, which enables it to reject all periodic disturbances which have the same period as the grid voltage, and whose highest frequency components are up to approximately 1.5 kHz.**

***Index Terms*—DC–AC power converter, H^∞ control, microgrid, repetitive control, total harmonic distortion (THD), voltage control.**

I. Introduction

FOR ECONOMIC, technical and environmental reasons, there is today a trend toward the use of small power generating units connected to the low-voltage distribution system in addition to the traditional large generators connected to the high-voltage transmission system [1]. Not only is there a change of scale but also a change of technology. Large generators are almost exclusively 50/60 Hz synchronous machines. Distributed power generators include variable speed (variable frequency) sources, high speed (high frequency) sources and direct energy conversion sources that produce dc. For example, wind-turbines are most effective if free to generate at variable frequency and so they require conversion from ac (variable frequency) to dc to ac (50/60 Hz) [2]; small gas-turbines with direct drive generators operate at high frequency and also require ac to dc to ac conversion [3]; photo-voltaic arrays require dc–ac conversion [4]. In all of these cases the same basic inverter (dc to ac converter) will be used and needs to be controlled to provide high-quality supply waveforms to consumers.

There are several operating regimes possible for distributed generation. One such is the microgrid in which the intention is that local consumers are largely supplied by local generation but that shortfalls or surpluses are exchanged through a connection to the public electricity supply system [5], [6]. The use of a microgrid opens up the possibility of making the distributed generator responsible for local power quality in a way that is not possible with conventional generators [7].

Manuscript received January 12, 2003; revised July 16, 2003. This paper was presented in part at the IEEE Conference on Decision and Control, Las Vegas, NV, December 10–13, 2002. This work was supported by EPSRC under Portfolio Partnership Grant GR/S61256/01. Recommended by Associate Editor B. Lehman.

The authors are with the Department of Electrical and Electronic Engineering, Imperial College London, London SW7 2BT, U.K. (e-mail: zhongqc@imperial.ac.uk).

Digital Object Identifier 10.1109/TPEL.2003.820561

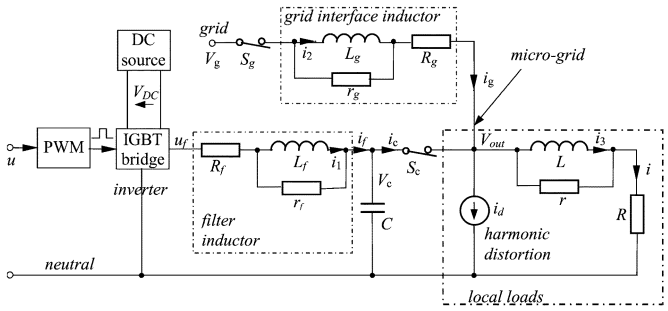

Fig. 1. Single-phase representation of the system to be controlled. The local loads are represented by a single linear load in parallel with a harmonic distortion current source. The PWM block is designed such that if $|u(t)| < V_{\rm DC}/2$ (no saturation), then the average of u_f over a switching period is the control input u.

Many of the loads connected to a distribution system or microgrid are nonlinear and create harmonically distorted current. The most common example is a linear load in series with a diode and with a dc-side capacitor. Many of the loads are also single-phase and so considerable zero-sequence and negative-sequence current components are expected. Because the grid has relatively high impedance at harmonic frequencies, the current distortion results in voltage distortion on the supply to adjacent customers. Allowing the converter in a generating unit to control the voltage of the microgrid will allow better power quality to be achieved. Fig. 1 shows the system to be controlled. The microgrid loads contain both linear and distorting elements. In Fig. 1, the loads have been lumped together into one linear load and a current sink which generates the harmonic components of the load current. The converter consists of a four-wire, three-phase inverter (IGBT bridge), an LC filter (to attenuate the switching frequency voltage components) and the controller. The microgrid can be supplied solely by the local generator, or solely by the grid, or by both in combination, or the local generator can both supply the microgrid and export power. Two isolators, S_c and S_g are provided to facilitate this and a grid interface inductor is provided to allow separation of the (sinusoidal) microgrid voltage and the (possibly distorted) grid voltage and also to facilitate the control of the real and reactive power exchange between the microgrid and the grid.

There are several aspects to the control of such a system.

1) DC-link balancing [8], [9]: to provide a neutral line, on which the voltage is balanced w.r.t. the two terminals of the dc link, even when the three-phase system is not balanced and there is a large zero-sequence current compo-

TABLE I
PARAMETERS OF THE SYSTEM

parameter	value	parameter	value
R_f	0.053Ω	R_g	0.1Ω
L_f	1.3mH	L_g	0.3mH
r_f	30.5Ω	r_g	7Ω
R	5Ω	C	50μF
L	5mH	V_g	$230V$, $50Hz$
r	500Ω	V_{DC}	$850V$

nent. A balanced dc link enables the voltage control of the three-phase converter to be decoupled into the voltage control of three single-phase converters.

2) Microgrid voltage control: to maintain a clean and balanced microgrid voltage in the presence of nonlinear loads and/or grid distortions. A small THD is a major objective of the voltage controller.
3) Power control: to regulate the (active and reactive) power exchange between the microgrid and the grid by generating a suitable reference voltage for the voltage controller [10].
4) Connection, disconnection and protection of the microgrid [11].
5) Discrete-time implementation of the controller using a digital signal processor.

This paper concentrates on one of these items only: microgrid voltage control. It is assumed that an outer control loop regulates the power exchange between the microgrid and the grid by developing appropriate reference voltages in terms of magnitude and phase shift with respect to the grid. These reference voltages for the three phases of the microgrid voltage are sinusoidal. It is then the task of the voltage controller to track accurately these reference voltages (so that the resulting THD is small). This controller will be subject to disturbances which include nonsinusoidal currents, changes in load current, changes and distortions in the grid voltage, and changes in the dc-link voltage.

Several control options exist. Conventional PI regulators can be used and have been widely reported in inverter control. In a rotating (dq) reference frame these regulators will seek to keep the dq voltage components at their dc reference values and suppress distortion that appears as higher frequency terms. These controllers can work well on balanced systems, but are not good at correcting unbalanced disturbance currents which are a common feature of distribution systems (and thus are not good at controlling single-phase converters). Such controllers are commonly employed for balanced three-phase motor loads. Regulators in a stationary reference frame can operate on a phase-by-phase basis and will have reasonable success at maintaining balanced voltages. The difficulty comes in designing a regulator with the correct gain against frequency characteristic to regulate the fundamental frequency and reject higher harmonic disturbances. PI regulators with their pole (infinite gain) at zero-frequency are not best suited to this task. A controller is required that has high gain at the fundamental and all harmonic frequencies of interest. Repetitive control [12]–[15] is such a control technique. In this paper, we design the voltage controller based on the H^∞ repetitive control theory developed in [12], leading to a very low harmonic distortion of the microgrid voltage even in the presence of nonlinear loads and/or grid distortions.

II. SYSTEM MODELING

The three-phase power system consists of the converter (including the IGBT bridge and LC filters), the local consumers, the grid interface inductor and the (external) power grid. Due to the presence of a balanced dc link (see [8], [9]), we may regard this system as three independent single-phase systems, as shown in Fig. 1, and hence there is no need to study here the three-phase behavior of the system. This assumption may be inaccurate, with coupling between the phases present in some consumers, but this coupling will not have any significant influence on the controller [10]. The filter inductor and other inductors in the system include two parasitic resistances: a series resistor to model winding resistance and a parallel resistor to model core losses. The resistance values we found from curve fitting experimental impedance data over the frequency range 50 Hz to 2 kHz.

The pulse-width-modulation (PWM) block is designed such that for $|u(t)| < V_{\rm DC}/2$, the local average of the bridge output voltage u_f equals u. This makes it possible to model the PWM block and the inverter with an average voltage approach. The PWM and inverter model is thus a simple saturated unity gain, where the saturation models the limit of the available dc-link voltage with respect to the neutral line ($\pm V_{\rm DC}/2$). The nominal active power in one phase of the load is 10 kW.

Our control objective is to maintain the microgrid voltage $V_{\rm out}$ as close as possible to the given sinusoidal reference voltage $V_{\rm ref}$, so that the THD of $V_{\rm out}$ is small. The two isolators S_c and S_g appearing in Fig. 1 are needed in the start-up and shut-down procedures of the converter, which will not be discussed in this paper, but some of it is discussed in [10]. In this paper, the switches are considered to be closed. The parameters of the system are shown in Table I. The switching frequency of the IGBT bridge is 10 kHz.

We take the state variables as the currents of the three inductors and the voltage of the capacitor ($V_c = V_{\rm out}$, since S_c is closed). The external input variables (disturbances and references) are i_d, V_g and $V_{\rm ref}$ and the control input is u. Thus

$$x = \begin{bmatrix} i_1 \\ i_2 \\ i_3 \\ V_c \end{bmatrix}, \quad \begin{bmatrix} w \\ \hline u \end{bmatrix} = \begin{bmatrix} i_d \\ V_g \\ V_{\rm ref} \\ \hline u \end{bmatrix}.$$

The state equations of the plant are

$$\dot{x} = Ax + [B_1 \quad B_2] \begin{bmatrix} w \\ u \end{bmatrix} \tag{1}$$

where you have the first equation shown at the bottom of the next page. The output signals from the plant are the tracking

error $e = V_{\text{ref}} - V_c$ and the current i_c, so that $y = [\, e \;\vdots\; i_c \,]^T$.

The output equations are

$$y = \begin{bmatrix} C_1 \\ C_2 \end{bmatrix} x + \begin{bmatrix} D_{11} & D_{12} \\ D_{21} & D_{22} \end{bmatrix} \begin{bmatrix} w \\ u \end{bmatrix} \tag{2}$$

where you have the second equation shown at the bottom of the page. The corresponding plant transfer function is

$$\mathbf{P} = \left[\begin{array}{c|cc} A & B_1 & B_2 \\ \hline C_1 & D_{11} & D_{12} \\ C_2 & D_{21} & D_{22} \end{array}\right] = [\mathbf{P}_{yw} \mathbf{P}_{yu}] \tag{3}$$

where we have used the compact notation now standard in control theory [16], [17], i.e., $\mathbf{P}(s) = C(sI - A)^{-1}B + D$.

III. Controller Design

We will follow the H^∞ control-based design procedure for repetitive controllers proposed in [12], which uses additional measurement information from the plant. The block diagram of the control system is shown in Fig. 2. The three external signals (the components of w) are assumed to be periodic, with a fundamental frequency of 50 Hz. The controller consists of an internal model $\mathbf{M}$ and a stabilizing compensator $\mathbf{C}$. The stabilizing compensator assures the exponential stability of the entire system and this implies that the error e will converge to a small steady-state error, according to the theory in [12].

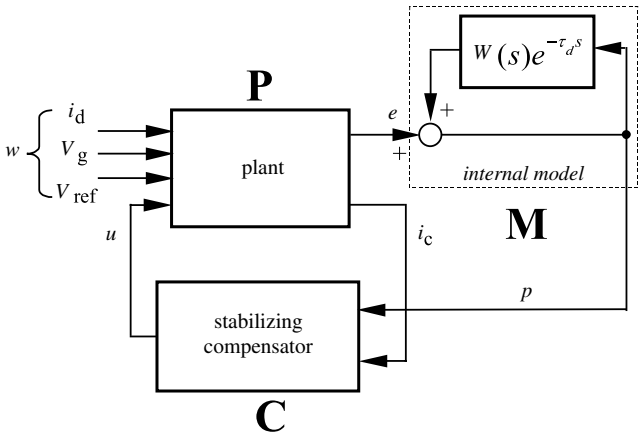

Fig. 2. Repetitive control system used for voltage tracking. Here, w is the disturbance and e is the tracking error. The plant is the average model of the system from Fig. 1.

As in [12], the internal model is obtained from a low-pass filter with transfer function $W(s) = (\omega_c/s + \omega_c)$ with $\omega_c = 10\,000$ rad/sec, cascaded with a delay element with transfer function $e^{-\tau_d s}$, where τ_d is slightly less than the fundamental period $\tau = 20$ msec

$$\tau_d = \tau - \frac{1}{\omega_c} = 19.9 \text{ ms}. \tag{4}$$

A realization of W is

$$W = \left[\begin{array}{c|c} A_w & B_w \\ \hline C_w & 0 \end{array}\right] = \left[\begin{array}{c|c} \omega_c & \omega_c \\ \hline 1 & 0 \end{array}\right].$$

$$A = \begin{bmatrix} -\frac{R_f r_f}{(R_f+r_f)L_f} & 0 & 0 & -\frac{r_f}{(R_f+r_f)L_f} \\ 0 & -\frac{R_g r_g}{(R_g+r_g)L_g} & 0 & -\frac{r_g}{(R_g+r_g)L_g} \\ 0 & 0 & -\frac{Rr}{(R+r)L} & \frac{r}{(R+r)L} \\ \frac{r_f}{(R_f+r_f)C} & \frac{r_g}{(R_g+r_g)C} & -\frac{r}{(R+r)C} & -\left(\frac{1}{R+r} + \frac{1}{R_f+r_f} + \frac{1}{R_g+r_g}\right)\frac{1}{C} \end{bmatrix}$$

$$B = [B_1 \quad B_2] = \left[\begin{array}{ccc|c} 0 & 0 & 0 & \frac{r_f}{(R_f+r_f)L_f} \\ 0 & \frac{r_g}{(R_g+r_g)L_g} & 0 & 0 \\ 0 & 0 & 0 & 0 \\ -\frac{1}{C} & \frac{1}{(R_g+r_g)C} & 0 & \frac{1}{(R_f+r_f)C} \end{array}\right]$$

$$C = \begin{bmatrix} C_1 \\ C_2 \end{bmatrix} = \left[\begin{array}{cccc} 0 & 0 & 0 & -1 \\ \hline 0 & -\frac{r_g}{R_g+r_g} & \frac{r}{R+r} & \frac{1}{R+r} + \frac{1}{R_g+r_g} \end{array}\right]$$

$$D = \begin{bmatrix} D_{11} & D_{12} \\ D_{21} & D_{22} \end{bmatrix} = \left[\begin{array}{ccc|cc} 0 & 0 & 1 & 0 & \\ \hline 1 & -\frac{1}{R_g+r_g} & 0 & 0 & \end{array}\right]$$

After closing a positive unity feedback around this cascade connection, as shown in Fig. 2, we obtain the internal model $\mathbf{M}$

$$\mathbf{M}(s) = \frac{1}{1 - e^{-\tau_d s}\mathbf{W}(s)}. \tag{5}$$

$\mathbf{M}$ has an infinite sequence of pairs of conjugate poles of which about the first 30 are very close to the imaginary axis, around integer multiples of $j2\pi \cdot 50 (j = \sqrt{-1})$, and the later ones are further to the left (see Appendix A for more details). The choice of ω_c is based on a compromise: for ω_c too low, only a few poles of the internal model will be close to the imaginary axis, leading to poor tracking and disturbance rejection at higher frequencies. For ω_c too high, the system is difficult to be stabilized (a stabilizing compensator may not exist, or it may need unreasonably high bandwidth).

According to [12], the closed-loop system in Fig. 2 is exponentially stable if the finite-dimensional closed-loop system from Fig. 3 is stable and its transfer function from a to b, denoted $\mathbf{T}_{ba}$, satisfies $\|\mathbf{T}_{ba}\|_\infty < 1$. The intuitive explanation for this is that in the control system of Fig. 2 a delay line is connected from the output b to the input a appearing in Fig. 3. To make this interconnected system stable, by the small gain theorem, it is sufficient to make the gain from a to b less than 1 at all frequencies.

Thus, we have to design $\mathbf{C}$ (the transfer function of the stabilizing compensator) such that the above two conditions are satisfied. Moreover, we want to minimize $(\gamma_0/1 - \gamma)$, where $\gamma_0 = \|\mathbf{T}_{ew}\|_\infty, \gamma = \|\mathbf{T}_{ba}\|_\infty < 1$. Indeed, we know from ([12] Section V) that a small value for $(\gamma_0)/(1 - \gamma)$ will result in a small steady-state error.

We formulate a standard H^∞ problem for the control system shown in Fig. 3, where $\tilde{w} = [v_1 v_2 w]^T$ and, in terms of Laplace transforms

$$\begin{bmatrix} \tilde{z} \\ \tilde{y} \end{bmatrix} = \tilde{\mathbf{P}} \begin{bmatrix} \tilde{w} \\ u \end{bmatrix}, \quad u = \mathbf{C}\tilde{y}.$$

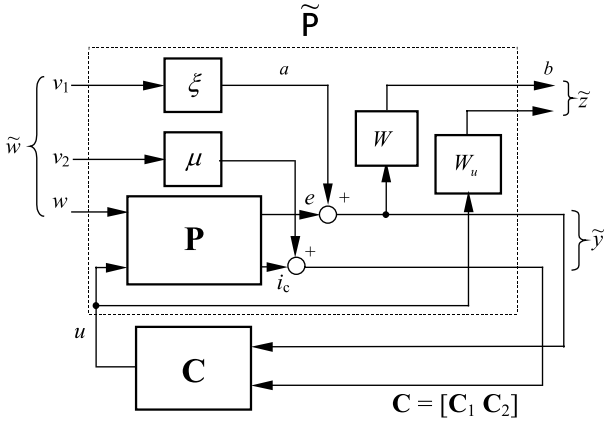

Fig. 3. Formulation of the H^∞ control problem. This block diagram represents an auxiliary problem and it is not equivalent to the one shown in Fig. 2. The extended plant $\mathbf{P}$ consists of the original plant $\mathbf{P}$ together with the filters W and W_u and the constant gains ξ and μ.

Here, ξ and μ are nonzero parameters whose choice gives us more freedom in the design. The small parameter μ is introduced to satisfy a rank condition needed to make the H^∞ problem solvable and

$$W_u = \left[\begin{array}{c|c} A_u & B_u \\ \hline C_u & D_u \end{array}\right]$$

is a weighting function whose value at infinity, $D_u = W_u(\infty) \neq 0$, is also needed for a rank condition. The problem formulation here is a slight improvement over the one in [12], where W_u was a constant. The fact that W_u is frequency-dependent allows us to choose it as a high-pass filter. This has the effect of reducing the controller gains at high frequencies. The extended plant $\tilde{\mathbf{P}}$ can be represented (see Appendix B) as (6) shown at the bottom of the page.

Using the μ-analysis and synthesis toolbox from MATLAB™ (the routine *hinfsyn*), we can find a controller $\mathbf{C}$ which nearly minimizes the H^∞-norm of the transfer matrix from $\tilde{w}$ to $\tilde{z}, \mathbf{T}_{\tilde{z}\tilde{w}} = \mathcal{F}_l(\tilde{\mathbf{P}}, \mathbf{C})$. However, this is *not* our final objective.

$$\tilde{\mathbf{P}} = \left[\begin{array}{ccc|ccc|c} A & 0 & 0 & 0 & 0 & B_1 & B_2 \\ B_w C_1 & A_w & 0 & B_w \xi & 0 & B_w D_{11} & B_w D_{12} \\ 0 & 0 & A_u & 0 & 0 & 0 & B_u \\ \hline 0 & C_w & 0 & 0 & 0 & 0 & 0 \\ 0 & 0 & C_u & 0 & 0 & 0 & D_u \\ \hline C_1 & 0 & 0 & \xi & 0 & D_{11} & D_{12} \\ C_2 & 0 & 0 & 0 & \mu & D_{21} & D_{22} \end{array}\right] \tag{6}$$

We denote the central sub-optimal controller for a given H^∞-norm of $\mathbf{T}_{\tilde{z}\tilde{w}}$ by

$$\mathbf{C} = \left[\begin{array}{c|cc} A_c & B_{c1} & B_{c2} \\ \hline C_c & 0 & 0 \end{array}\right] = [\mathbf{C}_1 \quad \mathbf{C}_2]$$

(note that its feedthrough matrix is equal to 0). After some manipulations (see Appendices C and D), we obtain the realizations of $\mathbf{T}_{ew}$ and $\mathbf{T}_{ba}$, respectively, as (7) and (8), shown at the bottom of the page. It is worth noting that (6)–(8) are valid for the general case, regardless of the dimension of the measurement vector, which here is the scalar i_c, and for any W and W_u.

Using the parameters shown in Table I, a nearly optimal controller, for which the Bode plots are shown in Fig. 4, was obtained for

$$W_u = \left[\begin{array}{c|c} -10\,000 & 1 \\ \hline -500 & 0.05 \end{array}\right], \quad W = \left[\begin{array}{c|c} -10\,000 & 10\,000 \\ \hline 1 & 0 \end{array}\right],$$
$$\xi = 37 \quad \text{and} \quad \mu = 0.5$$

(the latter two were determined via an extensive search to minimize $(\gamma_0)/(1-\gamma)$ while keeping $\gamma < 1$). The Bode plots show that this controller is not realistic, because it has a very large bandwidth. Normally, the high-frequency poles can be reduced using various controller/model reduction techniques, which is a topic of wide interest. Here, we use a different approach from that used in [18], [8], [9] to decrease the controller bandwidth: we do not minimize the H^∞-norm of $\mathcal{F}_l(\tilde{\mathbf{P}}, \mathbf{C})$ but find a sub-optimal controller $\mathbf{C}$ such that $||\mathcal{F}_l(\tilde{\mathbf{P}}, \mathbf{C})||_\infty \leq 25$ (which is larger than the minimal value 17.37). Such a controller (obtained using the *hinfsyn* routine in MATLAB is (9), shown at the bottom of the page. It is easy to check that $||\mathbf{T}_{ba}||_\infty < 1$ is satisfied for this $\mathbf{C}$. The pole p with the highest frequency creates a peak of the controller Bode plots at $|p| = \sqrt{3.07 \times 10^8} \approx 1.752 \times 10^4$ rad/sec, as can be seen in Fig. 5. This is well below half of the switching frequency $10{\times}10^3{\times}2\pi \approx 6.28{\times}10^4$ rad/s, which is the same as the sampling frequency of the processor used to implement the controller. We used this $\mathbf{C}$ as the stabilizing compensator in Fig. 2, for the simulations presented in the next section. We have also done simulations with the discretized controller (at the sampling frequency indicated above) and the results were very close to those for the continuous-time controller.

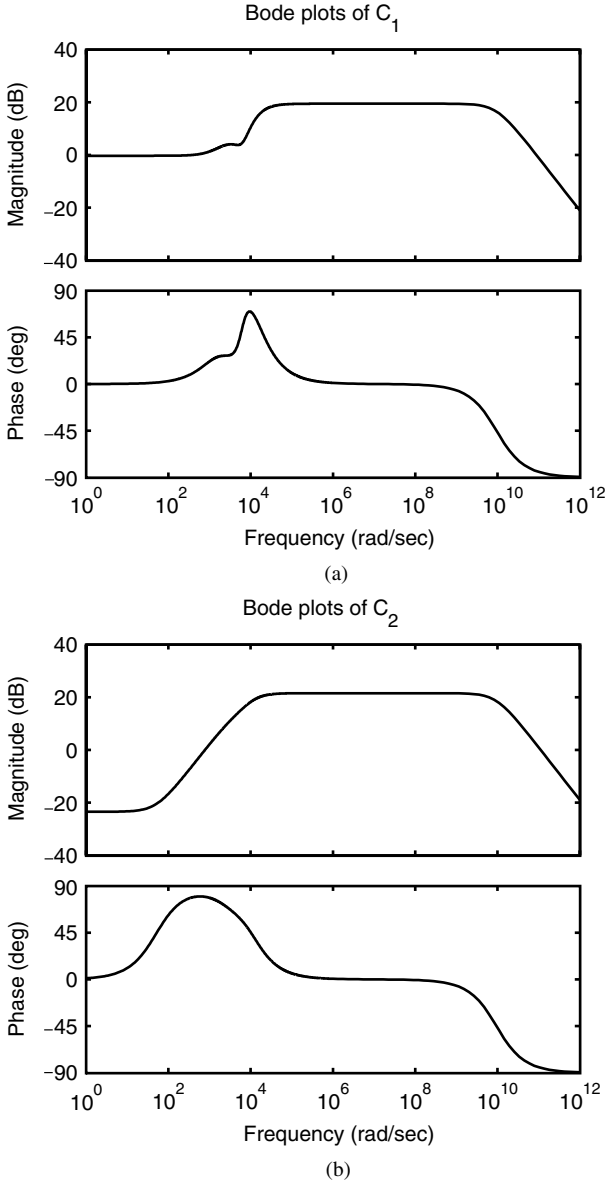

Fig. 4. Bode plots of a nearly optimal controller $\mathbf{C}$ for the H^∞ problem corresponding to Fig. 3. Note that it has a very large bandwidth, which is not realistic, given the switching frequency of 10 kHz. (a): Bode plots oc $\mathbf{C}_1$. (b) Bode plots oc $\mathbf{C}_2$.

$$\mathbf{T}_{ew} = \left[\begin{array}{cc|c} A & B_2C_c & B_1 \\ B_{c1}C_1 + B_{c2}C_2 & A_c + (B_{c1}D_{12} + B_{c2}D_{22})C_c & B_{c1}D_{11} + B_{c2}D_{21} \\ \hline C_1 & D_{12}C_c & D_{11} \end{array}\right] \tag{7}$$

$$\mathbf{T}_{ba} = \left[\begin{array}{cc|cc} A & B_2C_c & 0 & 0 \\ B_{c1}C_1 + B_{c2}C_2 & A_c + (B_{c1}D_{12} + B_{c2}D_{22})C_c & 0 & B_{c1} \\ B_wC_1 & B_wD_{12}C_c & A_w & B_w \\ \hline 0 & 0 & C_w & 0 \end{array}\right] \tag{8}$$

$$\mathbf{C}(s) = \left[\begin{array}{c} \frac{156\,751.405(s^2+2172s+1.185\times10^6)(s^2+5274s+3.767\times10^7)}{(s+9533)(s+2331)(s+989.2)(s^2+2.76\times10^4s+3.07\times10^8)} \\ \frac{266\,474.3105(s+10^4)(s+2958)(s+989.3)(s+20.43)}{(s+9533)(s+2331)(s+989.2)(s^2+2.76\times10^4s+3.07\times10^8)} \end{array}\right]^T \tag{9}$$

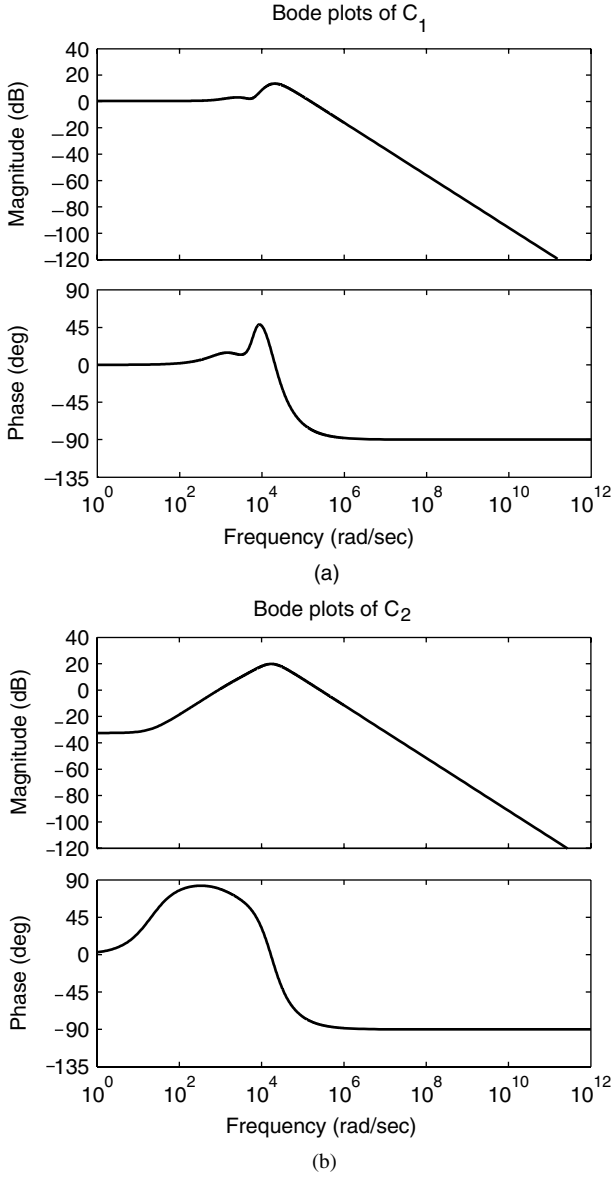

Fig. 5. Bode plots of the more realistic suboptimal controller $\mathbf{C}$ from (9). (a): Bode plots oc $\mathbf{C}_1$, (b) Bode plots oc $\mathbf{C}_2$.

The loop gain of the control system Fig. 2 is the transfer function $\mathbf{L}$ from u back to u. It is clear that

$$\mathbf{L} = \mathbf{C}\begin{bmatrix}\mathbf{M} & 0\\ 0 & 1\end{bmatrix}\mathbf{P}_{yu}$$

where $\mathbf{P}_{yu}$ is the plant transfer function from u to y from (3) and $\mathbf{M}$ is the internal model from (5). Hence

$$\mathbf{L} = \left[\begin{array}{c|c} A_c & B_{c1} \\ \hline C_c & 0 \end{array}\right]\left[\begin{array}{c|c} A & B_2 \\ \hline C_1 & D_{12} \end{array}\right]\mathbf{M} + \left[\begin{array}{c|c} A_c & B_{c2} \\ \hline C_c & 0 \end{array}\right]\left[\begin{array}{c|c} A & B_2 \\ \hline C_2 & D_{22} \end{array}\right].$$

The Nyquist plot of $-\mathbf{L}(j\omega)$ for $\omega \geq 0$ is shown in Fig. 6. We see that it is a complicated curve which does not encircle the critical point -1. The phase margin is about 40° and the gain margin is about 4.49 dB. Hence, the system has very good robustness w.r.t. to parameter uncertainties.

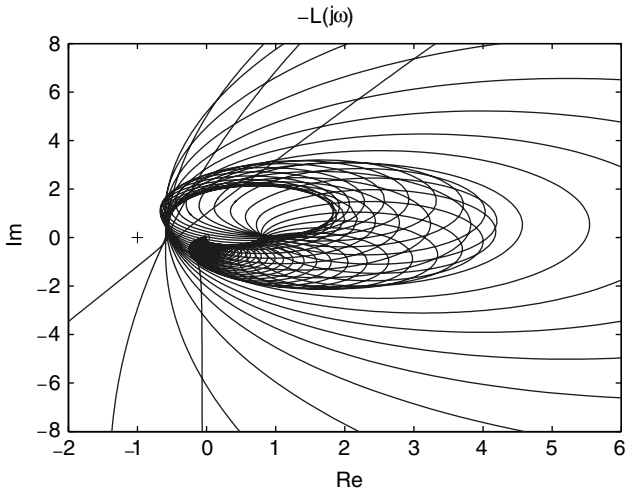

Fig. 6. Nyquist plot of $-\mathbf{L}(j\omega)$, where $\mathbf{L}$ is the loop gain (from u to u in Fig. 2), shown for $\omega \geq 0$. For $\omega \leq 0$, we obtain the complex conjugate curve, of course.

IV. Simulation Results

The simulations were done using Simulink in the MATLAB environment (similar results were obtained also in PSCAD). The solver used in the simulations was *ode23tb (stiff/TR-BDF2)* with variable steps. The maximal step size was 1 μs and the relative tolerance was 10^{-6}.

The phase of the grid voltage was assumed to be 0° and the power control loop was open, so that the voltage reference signal was $V_{\text{ref}} = 325 \sin \omega t$ V. Thus, in steady state and if the grid was undistorted, there was no power exchange between the microgrid and the grid. We have also run simulations with the power control loop working (see [10]), but here we omit those, since we do not want to burden this paper with the presentation of a power controller. From the point of view of voltage tracking, the results are similar, since the power control loop is much slower. As mentioned before, the voltage control of the three-phase converter has been decoupled into the voltage control of three independent single-phase converters. The neutral-leg controller (used for dc link balancing [8], [9]) will maintain a balanced neutral line even if the loads on the microgrid are not balanced. Hence, there is no need for simulations to show the three-phase behavior in this paper (but see [10], [11]).

A. Nominal Responses

Two simulations were conducted to assess the steady-state tracking performance of the system with the nominal load, with no disturbance current and an undistorted grid. The nominal load is shown in Fig. 1, with the values of the components as in Table I. The first simulation was conducted with the PWM block and the inverter modeled as a simple saturated unity gain with saturation levels of $\pm V_{\text{DC}}/2 = \pm 425$ V, as described in Section II. The output voltage and the tracking error, shown in Fig. 7(a), demonstrate that the tracking error reduces to very small values after approximately five mains cycles. The steady-state error, which is about 0.15 V(peak), is shown in Fig. 8(b).

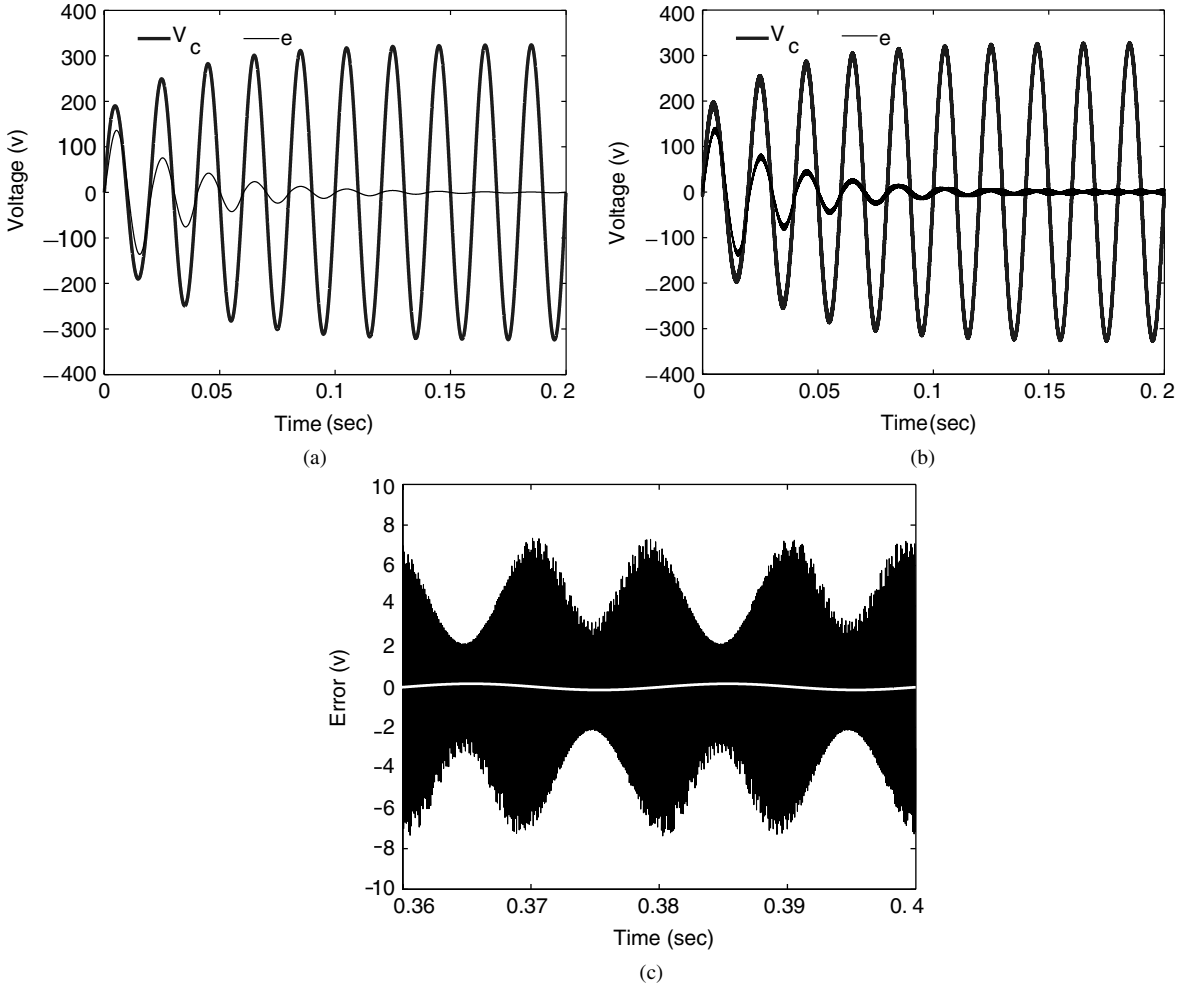

Fig. 7. Output voltage V_c and the tracking error e, without a current disturbance ($i_d = 0$) and with the nominal load. (a) With the PWM block and the inverter modeled as a simple saturation. (b) With a detailed (not average) model of the PWM block and the inverter ($f_s = 10$ kHz). (c) The steady-state tracking error simulated with a detailed model of the PWM block and the inverter. The white line shows the steady-state tracking error simulated with the PWM block and the inverter modeled as a unity gain with saturation, i.e., without switching noise.

The second simulation used a detailed inverter model including a PWM block, switching at 10 kHz. The response is shown in Fig. 7(b). The results are similar but there is switching noise present that increases the steady-state tracking error which now has ripples of approximately 7 V(peak), as shown in Fig. 7(c). The controller is unable to suppress the switching noise, because it can only update the input to the pulse-width modulator once per carrier cycle. The THD of the output voltage $V_c = V_{\text{out}}$ is around 1.37%, almost all due to the switching noise, as Fig. 7(c) shows.

We mention that the curves in Fig. 7(a) and (b) do not show the actual start-up process of an inverter with the nominal load, because the power controller is not present to ensure that the power changes smoothly from zero to the desired value. These curves only show the behavior of the voltage controller.

Fig. 8(b) shows the results of subjecting the plant to a disturbance current i_d shown in Fig. 8(a), which has the typical shape of the distortion caused by a capacitive rectifier. The peaks of i_d are about half the nominal load current. As can be seen, the system has a good capability to reject such a disturbance. Indeed, the output current i_c of the converter has a THD of 16.38%, but the THD of the microgrid voltage is only 0.16%. If we use a detailed model of the PWM block and the inverter, then the THD of i_c increases slightly to 16.45%, while the THD of the microgrid voltage becomes 1.39%.

B. Response to Load Changes

Simulations were done when the load is a pure resistor of 50 Ω, which absorbs about 10% of the load power used in the previous subsection. The PWM block and the inverter were still modeled as a saturation. The output voltage is shown in Fig. 9(a) and the tracking errors, with and without the disturbance current shown in Fig. 8(a), are shown in Fig. 9(b). No performance degradation can be observed from these figures (with respect to the nominal load).

A more involved simulation explored the transient responses when the load is changed from the nominal load to a pure resistor of 50 Ω. The tracking error and the current i_c are shown in Fig. 10. The load is changed at $t = 0.301$ s (when the load current is close to 0 so that the resulting spikes are small). The system reaches the steady state within fpur mains cycles and the dynamic error is less than 1.5 V. The response of the reverse process (changing the load from 50 Ω to the nominal load) is

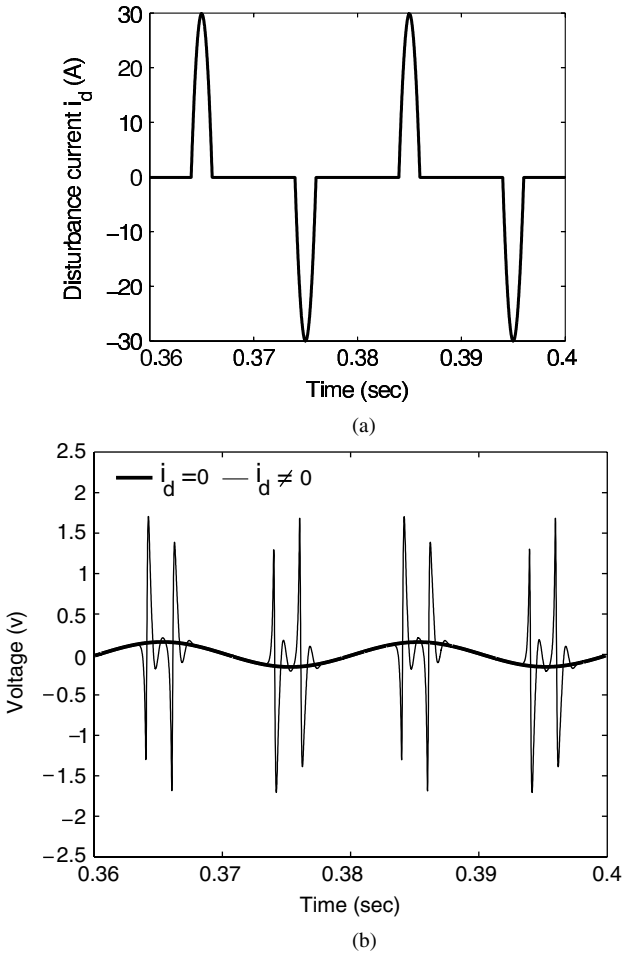

Fig. 8. Steady-state error for the nominal load with and without disturbance current (the PWM block and the inverter are modeled as a simple unity gain with saturation). (a) The disturbance current i_d. (b) The steady-state tracking error.

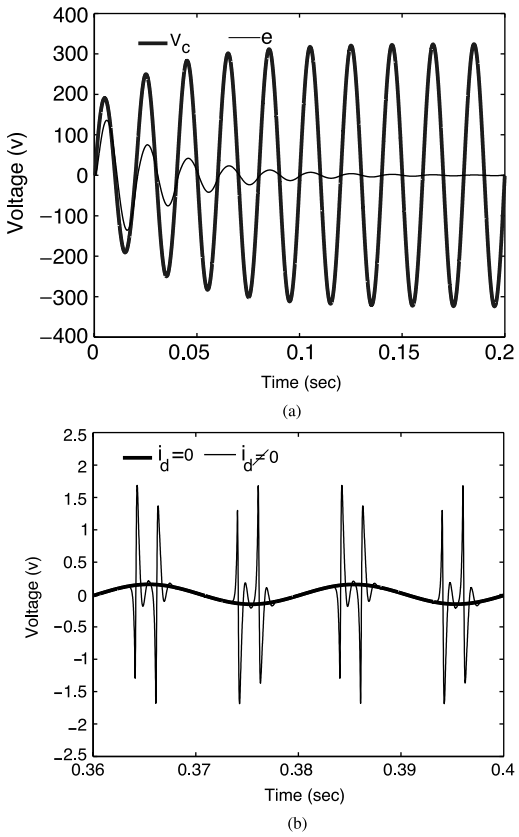

Fig. 9. Output voltage and the tracking error for a purely resistive load of 50 Ω with and without the disturbance current shown in Fig. 8(a) (the PWM block and the inverter are modeled as a simple saturation). (a) The output voltage and the error ($i_d = 0$). (b) The steady-state tracking error.

shown in Fig. 11. The system reaches the steady state within five mains cycles and the dynamic error is about than 1.5 V. In both simulations involving a change in the load, we took $i_d = 0$.

C. Response to Grid Distortions

A typical grid voltage is flattened at its peaks. Here, a grid voltage of $V_g = 325\sin\omega t - 32.5\sin 3\omega t - 32.5\sin 5\omega t$, as shown in Fig. 12(a), is used as an example. The tracking error decays rapidly, as shown in Fig. 12(b) and in the steady state it becomes very small (with ripples of about 7 V due to the effect of the PWM block). Although the external grid is extremely distorted, the microgrid is very clean, with a THD of about 1.20%, mostly due to the switching noise. In this simulation, the disturbance i_d is set to 0 and the load is the nominal load.

Another simulation was done when there was a shallow sag in the grid. The sag is −10% from 0.4 s to 0.6 s, as shown in Fig. 13(a). The tracking error is shown in Fig. 13(b). The maximal dynamic error is less than 6 V (peak) and the microgrid reaches the steady state within five mains cycles. In this simulation, $i_d = 0$ and the PWM block and the inverter are modeled as a saturation.

V. Conclusion

A control structure has been proposed for a dc–ac power converter connected to a microgrid with local loads and a public grid interface. The controller uses repetitive control on a per-phase basis in order to reject harmonic disturbances from nonlinear loads or the public grid. An H^∞ design method has been used to ensure that the controller performs effectively with a range of local load impedances. The system has been modeled and tested in Simulink and Matlab. The converter model includes a realistic switching frequency filter and a full model of the inverter PWM process. Our results have shown that, apart from the switching noise, the tracking of voltage references is accurate to within 0.15 V (for references of amplitude 325 V). The switching noise can have ripples of about 7 V, but there is nothing the controller can do to suppress this (high frequency) noise. If the load changes, the repetitive control loop converges (to a new limit cycle) and the tracking error becomes very small within approximately five mains cycles.

Appendix A
Poles of the Internal Model $\mathbf{M}$

The poles of the internal model $\mathbf{M}$ from (5) are the solutions of the transcendental equation

$$\frac{s+\omega_c}{\omega_c} = e^{-\tau_d s}$$

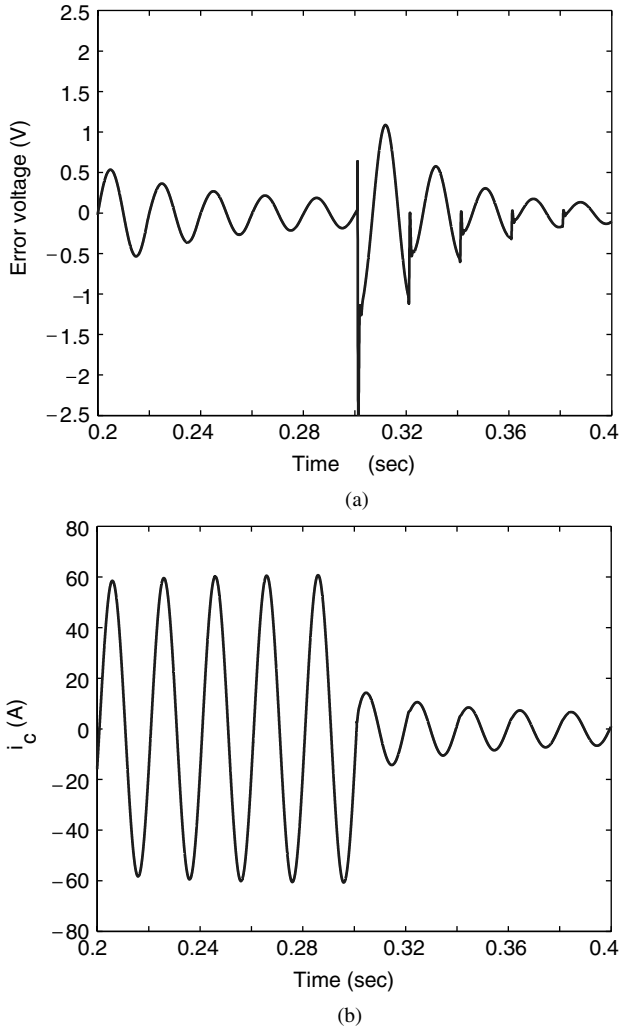

Fig. 10. Transient response when the load is changed at $t = 0.301$ s from the nominal load (as in Fig. 1) to a resistor of 50 Ω. There is no disturbance current and the PWM block and the inverter are modeled as a unity gain with saturation. (a) The tracking error voltage. (b) The load current.

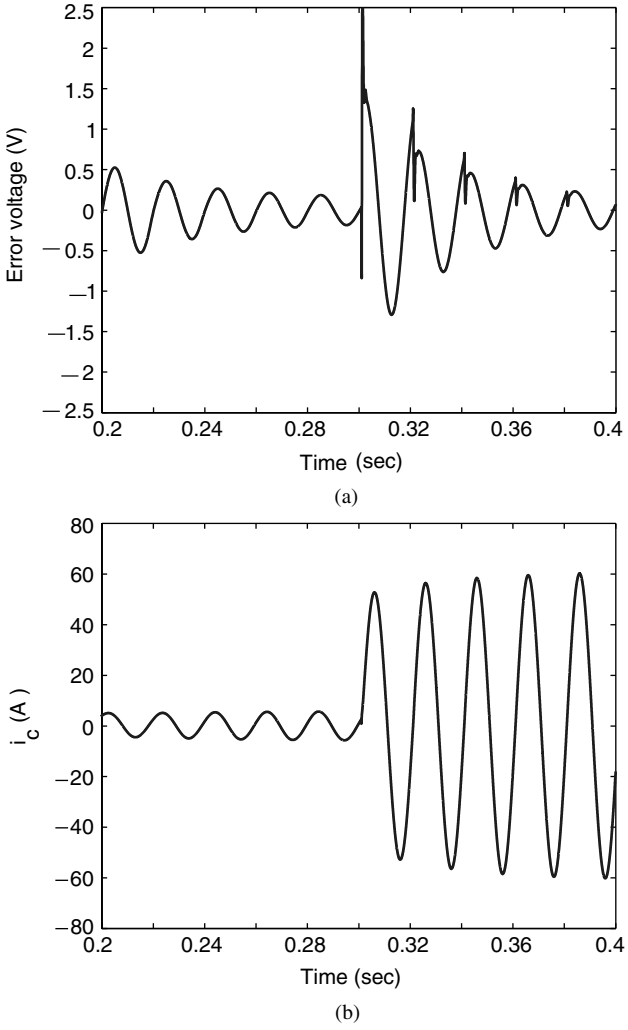

Fig. 11. Transient response when the load is changed at $t = 0.301$ s from a resistor of 50 Ω to the nominal load (as in Fig. 1). There is no disturbance current and the PWM block and the inverter are modeled as a unity gain with saturation. (a) The tracking error voltage. (b) The load current.

which has infinitely many roots $s_k, k \in \mathbb{Z}$. Substitute $s_k = \tilde{s}_k - \omega_c$, then $(1/\omega_c)\tilde{s}_k = e^{-\tau_d \tilde{s}_k} e^{\tau_d \omega_c}$, i.e.,

$$\tau_d \tilde{s}_k e^{\tau_d \tilde{s}_k} = \tau_d \omega_c e^{\tau_d \omega_c} = a. \tag{10}$$

We will need the *Lambert W function*, whose history and properties are beautifully presented in [19]. This is a multi-valued analytic function, with infinitely many branches denoted $W_k, k \in \mathbb{Z}$. The function W_k may be defined for $z \in \mathbb{C}\backslash(-\infty, 0]$ as the (unique) solution of

$$W_k(z) = \ln z + j2k\pi - \ln W_k(z) \tag{11}$$

where $\ln$ is the principal branch of the logarithm. Note that (11) implies that if $w = W_k(z)$ then $we^w = z$, which is the basic equation satisfied by all the branches W_k. For $z > 0, W_0(z)$ is the only positive solution of $we^w = z$. The (11) can be thought of as a fixed-point equation for the function

$$T_{k,z}(w) = \ln z + j2k\pi - \ln w.$$

For $k \neq 0$ and large $|z|$, the iterations defined by $w_{n+1} = T_{k,z}(w_n)$ converge fast to $W_k(z)$. The approximation formula (4.11) given in [19] can be written as $W_k(z) \approx T_{k,z}(T_{k,z}(1))$. Since for large real $z, W_0(z)$ is a better initial approximation of $W_k(z)$ than 1, we shall use the approximation

$$W_k(z) \approx T_{k,z}(T_{k,z}(W_0(z))) = \ln z + j2k\pi - \ln(\ln z + j2k\pi - \ln W_0(z)). \tag{12}$$

Now we return to the poles of $\mathbf{M}$. We see from (10) that

$$\tau_d \tilde{s}_k = W_k(a) \quad (k \in \mathbb{Z}), \quad \tau_d \omega_c = W_0(a)$$

so that

$$s_k = \frac{W_k(a) - \tau_d \omega_c}{\tau_d}. \tag{13}$$

Since a is large (in our design, $a = 199e^{199}$), $W_k(a)$ can be well approximated by (12), i.e.,

$$W_k(a) \approx \ln(\tau_d \omega_c) + \tau_d \omega_c + j2k\pi - \ln(\tau_d \omega_c + j2k\pi).$$

Now from (13)

$$\tau_d s_k \approx \ln(\tau_d \omega_c) - \ln \sqrt{(\tau_d \omega_c)^2 + (2k\pi)^2} + j\left(2k\pi - \tan^{-1} \frac{2k\pi}{\tau_d \omega_c}\right)$$

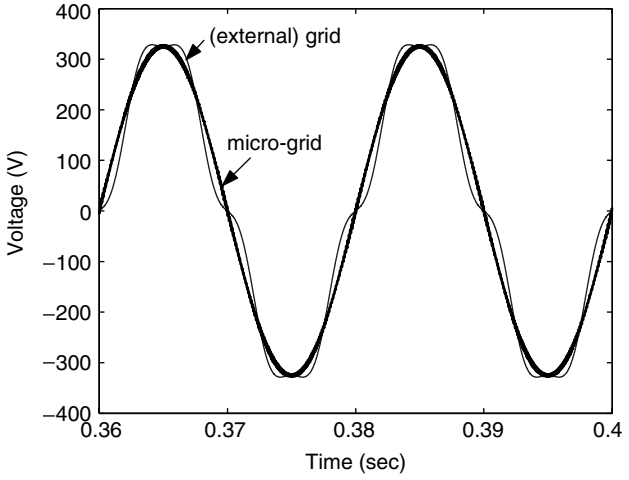

(a)

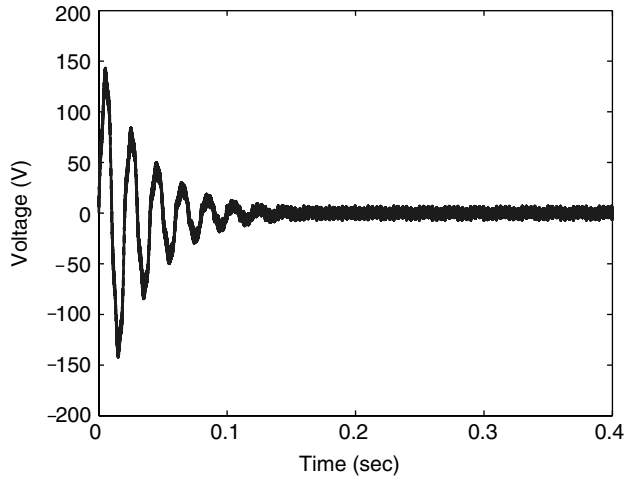

(b)

Fig. 12. Effect of a distorted public grid: the grid voltages and the tracking error. In this simulation, we have used a detailed model of the PWM block and the inverter. The switching noise is visible in the plot of the error. (a) The steady-state grid voltages. (b) The transient tracking error.

so that

$$\mathrm{Re}s_k \approx \frac{1}{\tau_d}\ln\frac{\tau_d\omega_c}{\sqrt{(\tau_d\omega_c)^2+(2k\pi)^2}} = -\frac{1}{2\tau_d}\ln\left(1+\left(\frac{2k\pi}{\tau_d\omega_c}\right)^2\right), \tag{14}$$

$$\mathrm{Im}s_k \approx \frac{2k\pi-\tan^{-1}\frac{2k\pi}{\tau_d\omega_c}}{\tau_d} \approx \frac{2k\pi}{\tau_d}\left(1-\frac{1}{\tau_d\omega_c}\right). \tag{15}$$

The last approximation holds because if $|(2k\pi/\tau_d\omega_c)| \ll 1$ then we may approximate $\tan^{-1}$ by the identity function. These approximated poles and the true poles are shown in Fig. 14 for $|k| \le 31$, and we have checked that the approximation is very good even for $|k| \le 1000$. Ideally, we would like to have $s_k = j(2\pi/\tau)k$. At least, we want this to be approximately true for small $|k|$. In order to make $\mathrm{Im}s_k \approx (2\pi/\tau)k$, according to (15), we need τ_d to satisfy $\tau_d^2 = \tau_d\tau - (1/\omega_c)\tau$. Solving this equation, we obtain

$$\tau_d = \frac{1 \pm \sqrt{1-\frac{4}{\omega_c\tau}}}{2}\tau. \tag{16}$$

The solution with a minus sign is not reasonable, since it would lead to $\tau_d\omega_c \approx 1$ and then many of the approximations used earlier would break down. The reasonable solution corresponds to the plus sign in (16) and then a good approximation of τ_d, when $\omega_c\tau$ is large, is

$$\tau_d \approx \frac{1+1-\frac{2}{\omega_c\tau}}{2}\tau = \tau - \frac{1}{\omega_c}$$

as in (4). This coincides with the recommendation in ([12], Section II). However, when $\omega_c\tau$ is not so large, τ_d should be chosen according to (16) with the plus sign.

Appendix B
Realization of $\tilde{\mathbf{P}}$

Here we derive (6), the realization of the extended plant. We have from Fig. 3

$$\begin{aligned}
\tilde{y}_1 &= e + \xi v_1 \\
&= \xi v_1 + \left[\begin{array}{c|cc} A & B_1 & B_2 \\ \hline C_1 & D_{11} & D_{12} \end{array}\right]\begin{bmatrix} w \\ u \end{bmatrix} \\
&= \left[\begin{array}{c|cccc} A & 0 & 0 & B_1 & B_2 \\ \hline C_1 & \xi & 0 & D_{11} & D_{12} \end{array}\right]\begin{bmatrix} v_1 \\ v_2 \\ w \\ u \end{bmatrix}, \\
\tilde{y}_2 &= i_c + \mu v_2 \\
&= \left[\begin{array}{c|cc} A & B_1 & B_2 \\ \hline C_2 & D_{21} & D_{22} \end{array}\right]\begin{bmatrix} w \\ u \end{bmatrix} + \mu v_2 \\
&= \left[\begin{array}{c|cccc} A & 0 & 0 & B_1 & B_2 \\ \hline C_2 & 0 & \mu & D_{21} & D_{22} \end{array}\right]\begin{bmatrix} v_1 \\ v_2 \\ w \\ u \end{bmatrix}, \\
\tilde{z}_1 &= W(\xi v_1 + e) \\
&= \left[\begin{array}{c|c} A_w & B_w \\ \hline C_w & 0 \end{array}\right]\left[\begin{array}{c|cccc} A & 0 & 0 & B_1 & B_2 \\ \hline C_2 & \xi & 0 & D_{11} & D_{22} \end{array}\right]\begin{bmatrix} v_1 \\ v_2 \\ w \\ u \end{bmatrix} \\
&= \left[\begin{array}{cc|cccc} A & 0 & 0 & 0 & B_1 & B_2 \\ B_wC_1 & A_w & B_w\xi & 0 & B_wD_{11} & B_wD_{12} \\ \hline 0 & C_w & 0 & 0 & 0 & 0 \end{array}\right]\begin{bmatrix} v_1 \\ v_2 \\ w \\ u \end{bmatrix}, \\
\tilde{z}_2 &= W_u \cdot u = \left[\begin{array}{c|cccc} A & 0 & 0 & 0 & B_u \\ \hline C_u & 0 & 0 & 0 & D_u \end{array}\right]\begin{bmatrix} v_1 \\ v_2 \\ w \\ u \end{bmatrix}.
\end{aligned}$$

If we combine the above equations, then we obtain (6).

Appendix C
Realization of $\mathbf{T}_{ew}$

Here we derive (7). Assume in Fig. 3 $v_1 = 0$ and $v_2 = 0$, then $u = C_cx_c$, where x_c satisfies

$$\dot{x}_c = A_cx_c + B_{c1}e + B_{c2}i_c.$$

Substitute $u = C_cx_c$ into (1), then

$$\dot{x} = Ax + B_2C_cx_c + B_1w$$

and from (2)

$$e = C_1x + D_{12}C_cx_c + D_{11}w,$$
$$i_c = C_2x + D_{22}C_cx_c + D_{21}w.$$

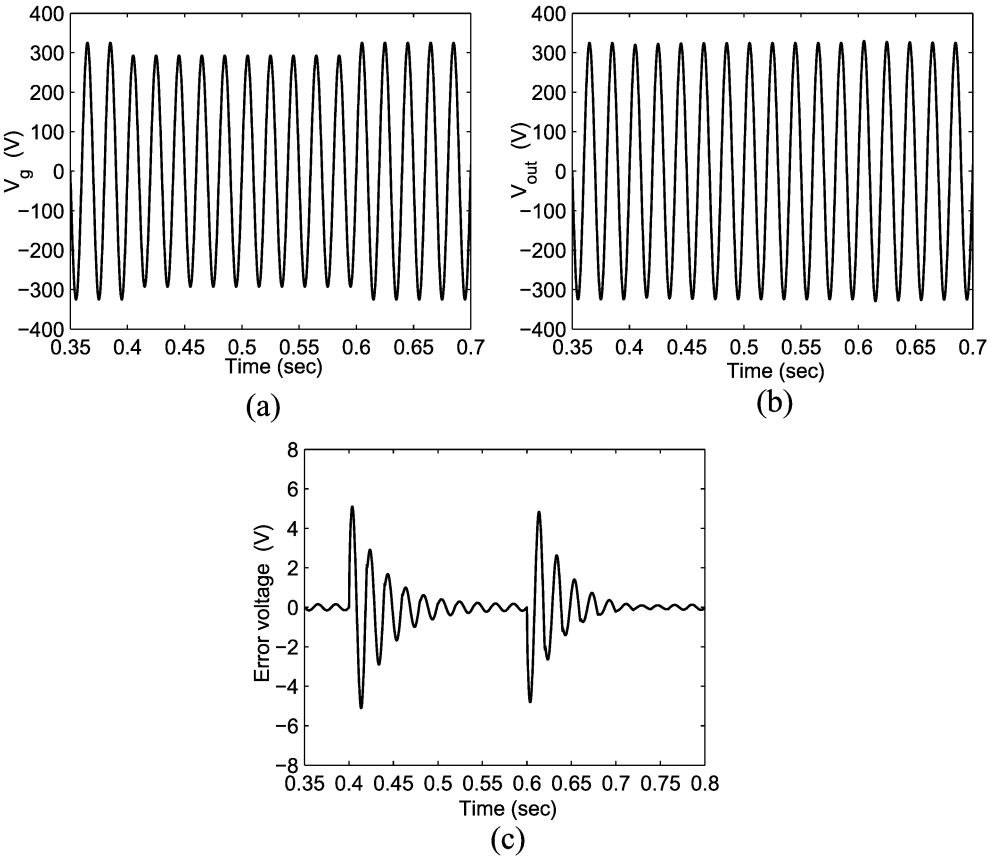

Fig. 13. Effect of a shallow sag of -10% in the grid voltage from $t = 0.4$ s to $t = 0.6$ s. (a) The (external) grid voltage. (b) The microgrid voltage. (c) The transient tracking error.

Furthermore

$$\dot{x}_c = (A_c + B_{c1}D_{12}C_c + B_{c2}D_{22}C_c)x_c + (B_{c1}C_1 + B_{c2}C_2)x + (B_{c1}D_{11} + B_{c2}D_{21})w.$$

Hence, the transfer matrix from w to e is the first equation at the bottom of the page.

APPENDIX D
REALIZATION OF $\mathbf{T}_{ba}$

Here we derive (8). Assume in Fig. 3 $w = 0$ and $v_2 = 0$, then

$$\dot{x} = Ax + B_2u, \quad e = C_1x + D_{12}u, \quad i_c = C_2x + D_{22}u$$

and $u = C_cx_c$, where

$$\begin{aligned}\dot{x}_c &= A_cx_c + B_{c1}(e + a) + B_{c2}i_c \\ &= A_cx_c + (B_{c1}C_1 + B_{c2}C_2)x \\ &\quad + (B_{c1}D_{12} + B_{c2}D_{22})C_cx_c + B_{c1}a\end{aligned}$$

so that $e + a = C_1x + D_{12}C_cx_c + a$. Hence, the transfer matrix from a to b is the second equation at the bottom of the page.

$$\mathbf{T}_{ew} = \left[\begin{array}{cc|c} A & B_2C_c & B_1 \\ B_{c1}C_1 + B_{c2}C_2 & A_c + (B_{c1}D_{12} + B_{c2}D_{22})C_c & B_{c1}D_{11} + B_{c2}D_{21} \\ \hline C_1 & D_{12}C_c & D_{11} \end{array}\right]$$

$$\mathbf{T}_{ba} = W\left[\begin{array}{cc|c} A & B_2C_c & 0 \\ B_{c1}C_1 + B_{c2}C_2 & A_c + (B_{c1}D_{12} + B_{c2}D_{22})C_c & B_{c1} \\ \hline C_1 & D_{12}C_c & 1 \end{array}\right]$$

$$= \left[\begin{array}{ccc|c} A & B_2C_c & 0 & 0 \\ B_{c1}C_1 + B_{c2}C_2 & A_c + (B_{c1}D_{12} + B_{c2}D_{22})C_c & 0 & B_{c1} \\ B_wC_1 & B_wD_{12}C_c & A_w & B_w \\ \hline 0 & 0 & C_w & 0 \end{array}\right]$$

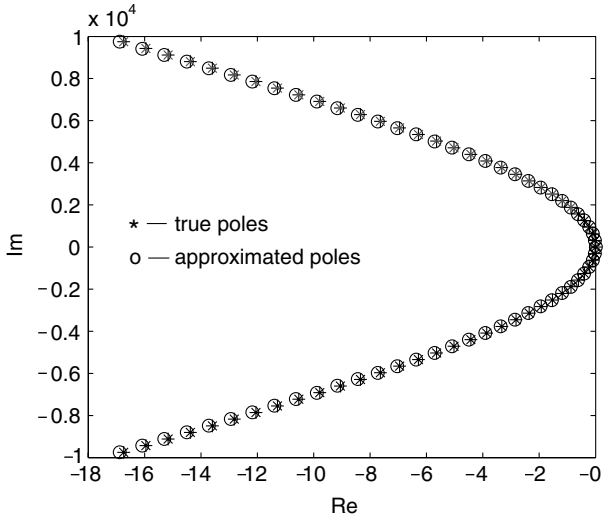

Fig. 14. Poles s_k of the internal model $\mathbf{M}$ for $|k| \leq 31$. Note that the horizontal scale is much smaller than the vertical scale, so that these poles are actually almost on the imaginary axis. Here, the approximation formulae (14)–(15) were used.

ACKNOWLEDGMENT

The authors wish to thank the Editors and the Reviewers for their careful work and helpful advice on this paper.

REFERENCES

[1] N. Jenkins, R. Allan, P. Crossley, D. Kirschen, and G. Strbac, *Embedded Generation*, ser. IEE Power and Energy Series: IEE Books, 2000.

[2] Z. Chen and E. Spooner, "Grid power quality with variable speed wind turbines," *IEEE Trans. Energy Conv.*, vol. 16, pp. 148–154, June 2001.

[3] M. Etezadi-Amoli and K. Choma, "Electrical performance characteristics of a new microturbine generator," in *Proc. IEEE Power Eng. Soc. Winter Meeting*, vol. 2, 2001, pp. 736–740.

[4] J. Enslin, M. Wolf, D. Snyman, and W. Swiegers, "Integrated photovoltaic maximum power point tracking converter," *IEEE Trans. Ind. Electron.*, vol. 44, pp. 769–773, Dec. 1997.

[5] R. Lasseter, "MicroGrids," *Proc. IEEE Power Eng. Soc. Winter Meeting*, vol. 1, pp. 305–308, 2002.

[6] G. Venkataramanan and M. Illindala, "Microgrids and sensitive loads," *Proc. IEEE Power Eng. Soc. Winter Meeting*, vol. 1, pp. 315–322, 2002.

[7] T. Green and M. Prodanović, "Control of inverter-based microgrids," *Electric Power Syst. Res., Special Issue Distributed Generation*, 2003.

[8] Q.-C. Zhong, T. Green, J. Liang, and G. Weiss, "H^∞ control of the neutral leg for three-phase four-wire dc–ac converters," in *Proc. 28th Annu. Conf. IEEE Ind. Electron. Soc. (IECON'02)*, Seville, Spain, Nov. 2002.

[9] Q.-C. Zhong and G. Weiss, "H^∞ control of the neutral leg for three-phase four-wire dc-ac converters," *IEEE Trans. Ind. Electron.*, submitted for publication.

[10] J. Liang, T. Green, G. Weiss, and Q.-C. Zhong, "Decoupling control of the active and reactive power for a grid-connected three-phase dc-ac inverter," in *Proc. Eur. Contr. Conf.*, Cambridge, MA, U.K., Sept. 2003.

[11] ——, "Evaluation of repetitive control for power quality improvement of distributed generation," in *Proc. 33rd IEEE Annu. Power Electron. Spec. Conf.*, vol. 4, Queensland, Autralia, June 2002, pp. 1803–1808.

[12] G. Weiss and M. Hafele, "Repetitive control of MIMO systems using H^∞ design," *Automatica*, vol. 35, no. 7, pp. 1185–1199, 1999.

[13] Y. Yamamoto, "Learning control and related problems in infinite-dimensional systems," in *Essays on Control: Perspectives in the Theory and Its Applications*, H. Trentelman and J. Willems, Eds. Boston, MA: Birkhäuser, 1993, pp. 191–222.

[14] K. Zhou, D. Wang, and K.-S. Low, "Periodic errors elimination in CVCF PWM dc/ac converter systems: Repetitive control approach," *Proc. Inst. Elect. Eng.*, vol. 147, no. 6, pp. 694–700, 2000.

[15] K. Zhou and D. Wang, "Digital repetitive learning controller for three-phase CVCF PWM inverter," *IEEE Trans. Ind. Electron.*, vol. 48, pp. 820–830, Aug. 2001.

[16] K. Zhou and J. Doyle, *Essentials of Robust Control*. Upper Saddle River, N.J.: Prentice-Hall, 1998.

[17] M. Green and D. Limebeer, *Linear Robust Control*. Englewood Cliffs, NJ: Prentice-Hall, 1995.

[18] R. Naim, G. Weiss, and S. Ben-Yaakov, "H^∞ control applied to boost power converters," *IEEE Trans. Power Electron.*, vol. 12, pp. 677–683, July 1997.

[19] R. Corless, G. Gonnet, D. Hare, D. Jeffrey, and D. Knuth, "On the Lambert W function," *Adv. Computat. Math*, vol. 5, pp. 329–359, 1996.

George Weiss received the Control Engineer degree from the Polytechnic Institute of Bucharest, Romania, in 1981 and the Ph.D. degree in applied mathematics from the Weizmann Institute, Rehovot, Israel, in 1989.

He has been with Brown University, Providence, RI, the Virginia Polytechnic Institute and State University, Blacksburg, the Weizmann Institute, Ben-Gurion University, Beer Sheva, Israel, the University of Exeter, U.K., and is currently with Imperial College London, U.K. His research interests are distributed parameter systems, operator semigroups, power electronics, repetitive control, and periodic (in particular, sampled-data) linear systems.

Qing-Chang Zhong was born in 1970 in Sichuan, China. He received the M.S. degree in electrical engineering from Hunan University, China, in 1997 and the Ph.D. degree in control theory and engineering from Shanghai Jiao Tong University, China, in 1999.

He started working in the area of control engineering in 1990 after graduating from the Xiangtan Institute of Mechanical and Electrical Technology (now renamed as Hunan Institute of Engineering). He held a postdoctoral position at Technion-Israel Institute of Technology, Israel, from 2000 to 2001. He is currently a Research Associate at the Department of Electrical and Electronic Engineering, Imperial College London, U.K. His current research focuses on H-infinity control of time-delay systems, control in power electronics, process control, control in communication networks, and control using delay elements such as input shaping technique and repetitive control.

Tim C. Green (M'89–SM'02) received the B.Sc. (with first class honors) degree from Imperial College, London, U.K., in 1986 and the Ph.D. degree from Heriot-Watt University, Edinburgh, U.K., in 1990, both in electrical engineering.

He was a Lecturer at Heriot Watt University, U.K., until 1994 and is now a Reader at Imperial College London and member of the Control and Power Research Group. His research interest is in using power electronics and control to enhance power quality and power delivery. This covers FACTS, active power filters, distributed generation and un-interruptible supplies.

Dr. Green is a Chartered Engineer in the U.K. and a member of the IEE.

Jun Liang (M'02) received the B.S. degree in electrical engineering from Huazhong University of Science and Technology, China, in 1992 and the M.S. and Ph.D. degrees in electrical engineering from the Electric Power Research Institute (EPRI), China, in 1995 and 1998, respectively.

He was with EPRI, from 1998 to 2001 as a Senior Engineer, and is currently a Research Associate in the Department of Electrical and Electronic Engineering, Imperial College London. His research interests are power electronics, power system control, renewable power generation, and distributed generation.